Synchronous-asynchronous laser mode-locking transition

Shang-Ying Wu,[1,*] Wei-Wei Hsiang,[2] and Yinchieh Lai[1,3,†]
[1]*Department of Photonics and Institute of Electro-Optical Engineering, National Chiao-Tung University, Hsinchu, Taiwan*
[2]*Department of Physics, Fu Jen Catholic University, Taipei, Taiwan*
[3]*Research Center for Applied Sciences, Academia Sinica, Taipei, Taiwan*
(Received 6 May 2015; published 27 July 2015)

Synchronous-asynchronous mode-locking transition in a hybrid active and passive mode-locked laser is investigated theoretically. Three distinct mode-locking states are found and their transition diagram under varying detuning frequency and modulation strength is determined. By examining the steady-state lasing gain as a function of the detuning modulation frequency, we also clarify why the laser will become unstable near the transition points and why the nonlinear saturable absorption effect is crucial for the stable asynchronous mode-locking operation.

DOI: 10.1103/PhysRevA.92.013848 PACS number(s): 42.55.Ah, 42.55.Wd, 42.60.Fc, 42.65.Sf

I. INTRODUCTION

Generation of high-repetition-rate optical pulse trains with short-pulse width is desirable for many new applications including ultrahigh-bit-rate coherent optical communication [1,2], optical analog-to-digital conversion [3,4], and wavelength-swept optical coherence tomography [5,6]. Active harmonic mode locking via intracavity amplitude modulation (AM) or phase modulation (PM) is the commonly used approach for enforcing the laser to operate at a high repetition rate [7–11]. The modulation frequency for active harmonic mode locking needs to be equal to the cavity fundamental repetition frequency multiplied by an integer so that the timing synchronization between the modulation and the pulse train circulated inside the cavity can be maintained. In contrast to the passive mode-locked laser, detuning of the active mode-locked laser exhibits many interesting laser nonlinear dynamics. For active AM mode-locked lasers, the laser will become chaoticlike when the detuning is large enough, mainly due to the large transient gain seen by the noise perturbations [12–16]. The laser may switch to the Q-switched mode-locking operation state as illustrated experimentally in [17]. For active PM (or FM) mode-locked lasers, the behavior of laser parameter changes in the presence of small modulation frequency detuning has been investigated theoretically [18]. Additionally, the FM oscillation operation state can be observed when the detuning is large enough [19–25], in which the light field is more like a cw light with a sinusoidally sweeping instantaneous frequency. The transition from mode locking to FM oscillation has been studied [23–25] and excess noises have been found near the state transition point.

The laser dynamics becomes more profound when the nonlinear passive mode-locking mechanisms are also involved. By utilizing the nonlinear polarization rotation effect for implementing equivalent fast saturable absorber action, the asynchronous mode-locking (ASM) operation state [26,27] has been recently demonstrated on both 10-GHz Er-doped [28,29] and Yb-doped harmonic mode-locked fiber lasers with active phase modulation [30]. Analyses based on the variational solution of the master equation have been carried out [28]. Some unique characteristics of the ASM operation state include the improved insensitivity to the detuning, slow periodic oscillation of the pulse timing and optical center frequency, better stability, and the possibility to achieve long-term stability through low-frequency electronics. However, the synchronous to asynchronous mode-locking transition under varying detuning frequency and modulation depth for this type of hybrid mode-locked lasers has not been explored carefully. It is the objective of the present work to carefully characterize the involved mode-locking states as well as their transition diagram.

In this study we begin by investigating the dynamical behavior of the laser pulse evolution under the modulation frequency detuning. The starting point for theoretical modeling is essentially based on the master equation for hybrid active and passive mode-locked lasers. Besides direct numerical simulation, the evolution equations of essential laser pulse parameters are also derived from the variational analysis [28,31–34] under the single-Gaussian-pulse solution ansatz for comparison and clarification purposes. The detuning behavior of the averaged difference between the steady-state gain and linear loss coefficients is examined to distinguish the transition of different laser operation states. By comparing the results under different operation conditions with and without the nonlinearity, we verify that the equivalent saturable absorption effect is crucial for the stable asynchronous mode-locking operation. The Kerr nonlinearity alone is not enough to efficiently achieve this purpose. Furthermore, the phase modulation strength can also essentially affect the transition of different mode-locking states. To investigate this correspondence, we have executed the two-dimensional (2D) parameter scanning for the modulation strength and the frequency detuning. The obtained 2D state transition diagram helps to clarify the scenario of the synchronous to asynchronous mode-locking transition. The analysis presented here also demonstrates an effective approach to elucidate the nonlinear mode-locked laser dynamics caused by the detuning effects and to predict the performance of the studied mode-locked laser systems under different operational conditions.

II. THEORETICAL MODEL

As illustrated in Fig. 1, the considered mode-locked fiber laser configuration in the present work is a hybrid active

*sywu123.eo99g@nctu.edu.tw
†yclai@mail.nctu.edu.tw

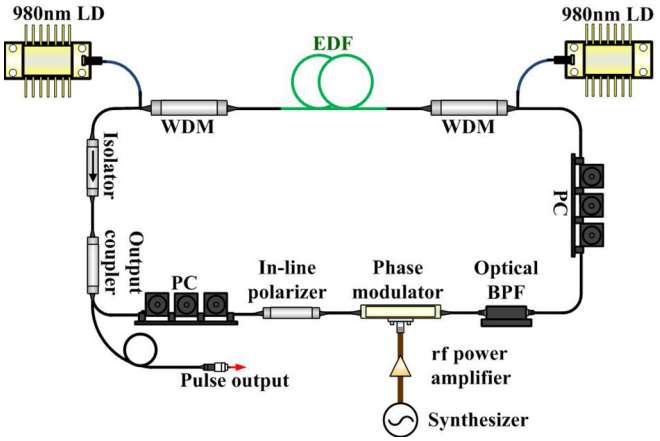

FIG. 1. (Color online) Schematic of the considered fiber laser system: LD, laser diode; PC, polarization controller; WDM, 980 − 1550 nm wavelength division multiplexer; EDF, Er-doped fiber; and BPF, bandpass filter.

and passive harmonic mode-locked Er-doped fiber laser with 10-GHz phase modulation [28,29]. The passive mode-locking effect is through the nonlinear polarization rotation mechanism, while the active mode-locking effect is through the phase modulation. The net cavity dispersion is anomalous so that the laser can operate in the soliton regime. For this type of mode-locked fiber lasers, the pulse width is typically on the picosecond order with the optical bandwidth on the order of a few nanometers. Thus both the intracavity dispersive and nonlinear effects are moderate and the assumption of small intracavity changes should be reasonably valid. Under this assumption, the pulse evolution in a hybrid active and passive mode-locked laser system with a detuned phase modulation frequency can be modeled by the following master equation [27,28]:

$$\frac{\partial U(T,t)}{\partial T} = [g(T) - l]U(T,t) + (d_r + jd_i)\frac{\partial^2 U(T,t)}{\partial t^2} + (k_r - jk_i)|U(T,t)|^2 U(T,t) - jM\{\cos[\omega_M(t + RT)]\}U(T,t). \quad (1)$$

Here $U(T,t)$ is the slowly varying field envelope, T is the number of the cavity round-trips for the long-time scale, and t is the short-time scale. The gain coefficient is given by $g(T) = g_0[1 + \int |U(T,t)|^2 dt/E_S]^{-1}$, where g_0 is the linear gain and E_S is the gain saturation energy. In addition, l is the linear loss, d_r is the effect of optical filtering, d_i is related to the net cavity dispersion, k_r is the equivalent fast saturable adsorption effect, k_i is the Kerr nonlinear effect, M is the strength of phase modulation, and ω_M is the angular modulation frequency. The linear timing walkoff per cavity round-trip due to the detuning frequency of phase modulation is given by $R = df/(f_R f_M)$, where df is the deviation frequency between the Nth cavity harmonic frequency Nf_R and the modulation frequency f_M. Here f_R is the fundamental cavity repetition frequency. We have numerically solved the master equation by using the fourth-order Runge-Kutta in the interaction picture (RK4IP) algorithm [35–37]. With the interaction picture transformation, the terms of dispersion and optical filtering can be separated from the nonlinear and modulation terms for more accurate numerical evaluation under a higher-order finite-difference scheme.

The typical simulation parameters used in the present study are $g_0 = 5$, $E_S = 0.77\,\text{pJ}$, $l = 1$, $d_r = 0.012\,\text{ps}^2$, which corresponds to the Gaussian filtering bandwidth of 13.5 nm (assumed centered at 1.55 μm), $d_i = -0.03\,\text{ps}^2$, $k_r = 0.003\,\text{W}^{-1}$, $k_i = 0.045\,\text{W}^{-1}$, $M = 0.8$, $f_R = 8\,\text{MHz}$, and $f_M = 10\,\text{GHz}$. These values should be reasonably close to the actual harmonic mode-locked Er-doped fiber lasers that can be experimentally built. The periodic boundary condition has been imposed and the simulation window size is set to be 100 ps, which is exactly one period of the 10-GHz pulse train. The initial condition is a chirpless Gaussian pulse with a pulse width of 10 ps and a pulse energy of 2 pJ.

III. LASER DYNAMICS

A. Pulse evolution under frequency detuning

As illustrated in Fig. 2, when the laser is operating under the synchronous mode-locking condition with zero detuning ($df = 0\,\text{kHz}$), the calculated solution is with the steady full width at half maximum (FWHM) pulse width $\tau_{\text{FWHM}} \approx 1.6\,\text{ps}$ and the pulse energy $E_P \approx 3\,\text{pJ}$ under the assumed 10-GHz repetition frequency. Since the pulse is synchronized with the modulation phase, the evolution plot in Fig. 2 for the $df = 0$ case is not moving when the steady state is reached. With a slight detuning of $df = 4\,\text{kHz}$, the modulation phase is now slowly moving with respect to the simulation window. Synchronous mode locking can still be maintained for this small detuning. In the evolution plot of Fig. 2(a) for this case, the pulse is moving with a constant timing drift per round-trip with respect to the simulation window and synchronized with the moving of the modulation phase. Physically this is achieved through the central wavelength shift of the pulse as shown in Fig. 2(b), such that the group velocity of the pulse can be changed sequentially to maintain the appropriate synchronous condition. When the detuning is increased to $df = 10\,\text{kHz}$, the synchronous mode locking is still maintained but the apparent intensity and spectral oscillation appear in the evolution plots. This indicates that the single-pulse mode-locking state now become not exactly stable. By examining the time evolution plot carefully, we believe that this oscillating behavior is essentially attributed to the growth of adjacent perturbation induced by the transient gain in the presence of detuning. With large enough detuning, the perturbation adjacent to the pulse has the chance to grow through the large transient gain and eventually becomes a new pulse with the simultaneous vanishing of the original pulse due to gain competition. This shows up in Fig. 2(a) as the quasiperiodic breakup of the evolution line. The slight timing shift near the breakup points can also be clearly observed. A more clearer evolution plot is shown in Fig. 3. In comparison to AM mode-locked lasers, a different kind of instability occurs under detuning.

At $df = 12\,\text{kHz}$, the synchronous mode-locked pulse is obtained again but the pulse width is longer, the pulse chirp is higher, and the shift of the center frequency is moved to the opposite site. This suggests that the laser is switched to a new synchronous mode-locking state. When the detuning

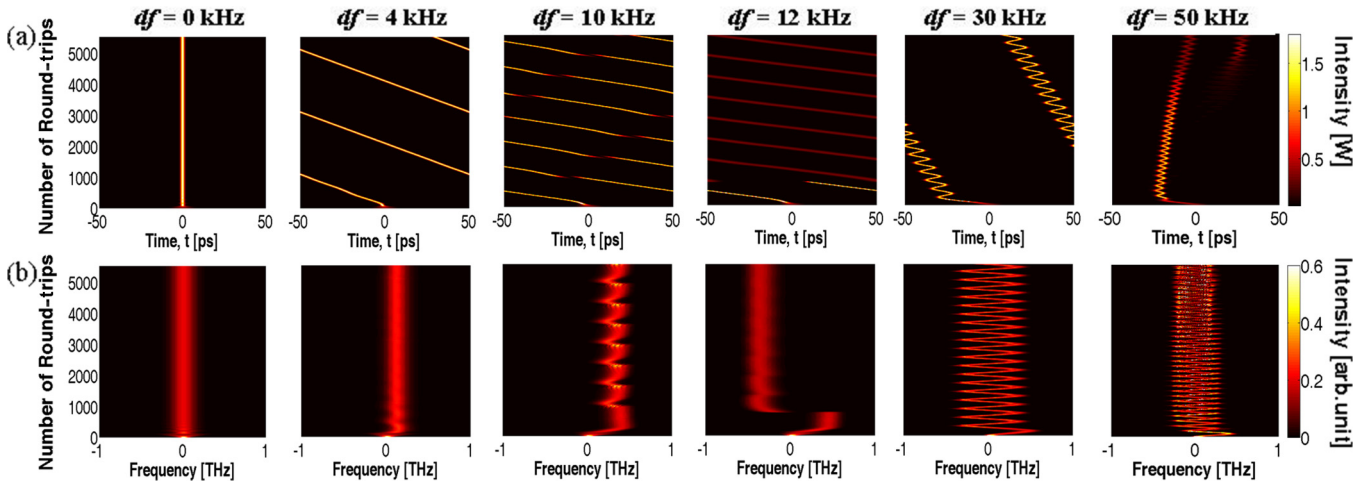

FIG. 2. (Color online) Calculated power distribution (a) in the time domain and (b) in the frequency domain under different detuning conditions with $df = 0$, 4, 12, 30, and 50 kHz.

frequency is further increased, similar oscillating behavior begins to show up before entering the ASM operation, indicating that this single-pulse mode-locking state is also not exactly stable. When the detuning is increased to $df = 20$ kHz, the ASM operation is observed. The short-pulse solution with clear sinusoidal timing position and center frequency oscillation can be observed as shown in Fig. 2 for the $df = 30$ kHz case. The laser is asynchronously mode locked in the sense that the pulse is not synchronized with the modulation and actually travels across the whole modulation phase slowly. One can see that the pulse still exhibits a much smaller but nonzero linear timing drift with respect to the simulation window, which is due to the repetition frequency pulling effect studied in [29]. The effect is dependent on the detuning frequency as illustrated in Fig. 4. Near the transition point the linear timing drift is larger. It decreases to be near zero when the detuning is increased. In Fig. 2, when the detuning is further increased to $df = 50$ kHz, the solution eventually becomes not mode locked. Transient pulse breakup can be observed in the time domain, while spectral oscillation can be clearly observed in the frequency domain.

To more clearly demonstrate the mode-locking state transition, the fundamental pulse parameters including the center angular frequency ω, the FWHM spectral bandwidth λ_{FWHM}, the pulse width τ_{FWHM}, the peak power $|U|^2_{\mathrm{peak}}$, and the pulse chirp C are plotted in Fig. 5 as a function of the detuning df. These pulse parameters are calculated from the pulse envelope solution by using the moment expressions derived in [38] and then averaged over a sufficient amount of round-trip time since the pulse envelope solution may be oscillating in general. From the plots it can be clearly seen that there are three distinct mode-locking states: synchronous short-pulse, synchronous long-pulse, and asynchronous short-pulse states.

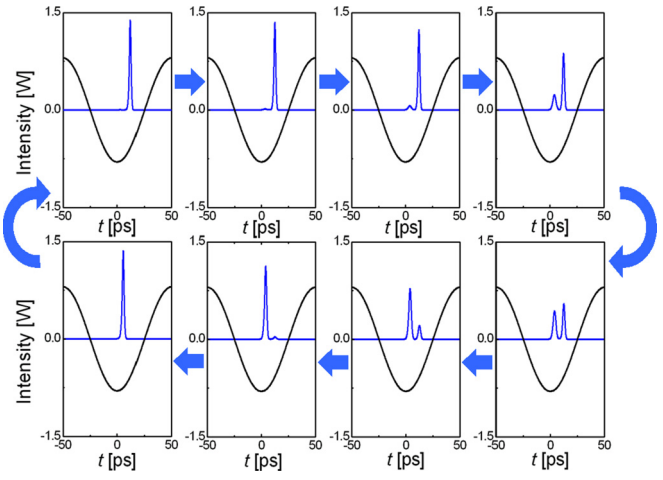

FIG. 3. (Color online) Occurrence of oscillation for a short pulse at $df = 10$ kHz. The blue line shows the short pulse and the black line the phase modulation curve. The time coordinate is transformed to be synchronized with the modulation phase to better illustrate the effect.

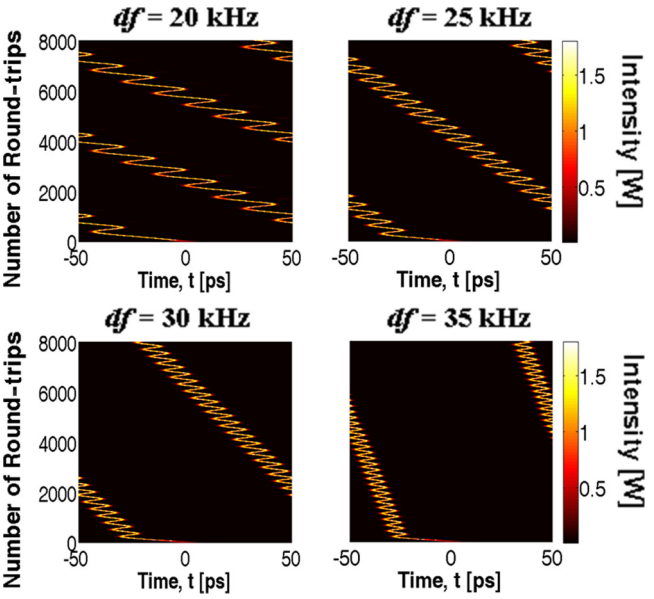

FIG. 4. (Color online) Calculated power distribution in the time domain under the asynchronous mode-locking operation with $df = 20$, 25, 30, and 35 kHz.

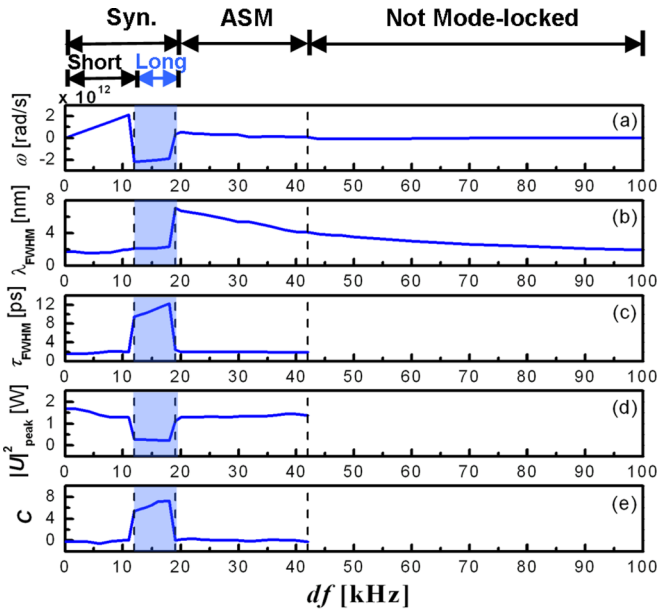

FIG. 5. (Color online) Averaged pulse parameters under different detuning: (a) the center angular frequecy ω of the optical spectrum, (b) the FWHM bandwidth of the optical spectrum λ_{FWHM}, (c) the FWHM pulse width τ_{FWHM}, (d) the pulse peak power $|U|^2_{\mathrm{peak}}$, and (e) the pulse chirp C.

The two short-pulse states are with a low chirp, while the long-pulse state is with a high chirp. The center frequency shift of the synchronous short-pulse state is linearly increased when the detuning effect is increased. The center frequency shift is switched to the opposite sign when entering the synchronous long-pulse state and relaxed back to be near zero when entering the ASM state. In contrast, the spectral bandwidth only exhibits a significant jump between the synchronous and asynchronous mode-locking operations. These distinct characteristics clearly indicate that the three mode-locking states are fundamentally different.

B. Variational single-pulse solution

To clarify theoretically the mode-locking pulse properties of the studied laser, we also reformulate the master equation (1) as a variational equation problem and then solve it approximately under the single-pulse solution ansatz [28,31–34]. Based on the variational principle, the Lagrangian function corresponding to Eq. (1) can be defined as follows:

$$\begin{aligned} L = {} & \frac{j}{2}\left(U\frac{\partial U^*}{\partial T} - U^*\frac{\partial U}{\partial T}\right) + d_i\left|\frac{\partial U}{\partial t}\right|^2 \\ & + \frac{k_i}{2}|U|^4 - m_2[t - t_0(T)]^2|U|^2 \\ & + jd_r\left(\frac{\partial^2 U_0}{\partial t^2}U^* - \frac{\partial^2 U_0^*}{\partial t^2}U\right) + j[k_r|U_0|^2 + (g-l)] \\ & \times(U_0U^* - U_0^*U) - m_1[t - t_0(T)](U_0U^* + U_0^*U). \end{aligned} \quad (2)$$

Here the sinusoidal phase modulation function of Eq. (1) has been expanded by a Taylor series at the pulse center to second order

$$M\cos[\omega_M(t+RT)] \approx m_0 - m_1[t - t_0(T)] - m_2[t - t_0(T)]^2. \quad (3)$$

The functions m_1 and m_2 are given by

$$m_1 = M\omega_M \sin\{\omega_M[t_0(T) + RT]\}, \quad (4)$$

$$m_2 = \frac{M}{2}\omega_M^2 \cos\{\omega_M[t_0(T) + RT]\}. \quad (5)$$

This approximation is appropriate when the laser pulse width is much shorter than the modulation time period. The master equation (1) can be derived from the Lagrangian function by taking the variation of the functional $I = \iint L dT dt$ with respect to U and U^*,

$$\delta I = \delta \iint L\left(U, U^*, \frac{\partial U}{\partial T}, \frac{\partial U^*}{\partial T}, \frac{\partial U}{\partial t}, \frac{\partial U^*}{\partial t}\right) dT dt = 0, \quad (6)$$

which should reproduce the master equation through the implied Euler-Lagrange equation

$$\frac{\partial L}{\partial U^*} - \frac{\partial}{\partial t}\frac{\partial L}{\partial(\partial U^*/\partial t)} - \frac{\partial}{\partial T}\frac{\partial L}{\partial(\partial U^*/\partial T)} = 0. \quad (7)$$

It should be noted that the functions U_0 and U_0^* in Eq. (2) should be handled as fixed functions and should not participate in the variational procedure. However, they should be replaced by the steady state solution and its complex conjugate, respectively, after accomplishing the variational derivation. This is a standard technique for dealing with loss terms under the variational formulation since all the nonconserved terms cannot be handled directly in the Lagrangian formulation. To analyze the mode-locked lasers, one reasonable pulse solution ansatz is the Gaussian pulse shape

$$\begin{aligned} U(T,t) = {} & \left(\frac{2}{\pi}\right)^{1/4} a(T)\exp\left(-[1 + jC(T)]\frac{[t - t_0(T)]^2}{\tau(T)^2}\right) \\ & \times e^{j\{\omega(T)[t - t_0(T)] + \theta(T)\}}. \end{aligned} \quad (8)$$

The physical meanings of the introduced parameters are as follows: $a(T)$ is the pulse amplitude, $\tau(T)$ is the pulse width, $t_0(T)$ is the pulse timing, $C(T)$ is the chirp, $\omega(T)$ is the pulse center frequency, and $\theta(T)$ is the phase. The evolution equations for all the pulse parameters can be derived from the approximate variational equation defined by the reduced Lagrangian $\langle L\rangle$,

$$\delta \int \langle L\rangle dT = 0, \quad (9)$$

where

$$\langle L\rangle = \int_{-\infty}^{\infty} L_{\mathrm{ansatz}} dt. \quad (10)$$

Here L_{ansatz} is derived from the Lagrangian function L by substituting the solution ansatz for the functions U and U^*. Thereafter, one can find the evolution equations of the pulse parameters from the corresponding Lagrange equations

$$\frac{\partial\langle L\rangle}{\partial x_i} - \frac{\partial}{\partial T}\frac{\partial\langle L\rangle}{\partial(\partial x_i/\partial T)} = 0. \quad (11)$$

Here x_i represents different pulse parameters in the solution ansatz. The derived evolution equations for the amplitude $a(T)$, the pulse width $\tau(T)$, the center frequency $\omega(T)$, the timing $t_0(T)$, and the chirp $C(T)$ are given by

$$\frac{da(T)}{dT} = [g(T) - l]a(T) - d_r\left[\omega(T)^2 + \frac{2}{\tau(T)^2}\right]a(T) + \frac{2d_iC(T)}{\tau(T)^2}a(T) + \frac{5k_ra(T)^2}{4\sqrt{\pi}}a(T), \quad (12)$$

$$\frac{d\tau(T)}{dT} = \frac{2d_r[1 - C(T)^2]}{\tau(T)} - \frac{4d_iC(T)}{\tau(T)} - \frac{k_ra(T)^2}{2\sqrt{\pi}}\tau(T), \quad (13)$$

$$\frac{d\omega(T)}{dT} = m_1 - \frac{4d_r[1 + C(T)^2]}{\tau(T)^2}\omega(T), \quad (14)$$

$$\frac{dt_0(T)}{dT} = 2d_rC(T)\omega(T) + 2d_i\omega(T), \quad (15)$$

$$\frac{dC(T)}{dT} = -m_2\tau(T)^2 - \frac{4[d_rC(T) + d_i][1 + C(T)^2]}{\tau(T)^2} - \frac{[k_rC(T) + k_i]a(T)^2}{\sqrt{\pi}}. \quad (16)$$

The evolution equation for the phase $\theta(T)$ is irrelevant to the following analysis and thus is omitted. The detuning effect is introduced in the functions of m_1 in Eq. (4) and m_2 in Eq. (5), where a linear drift term has been included.

As an application of the theory, under the synchronous mode-locking assumption, Eq. (15) for the pulse timing $t_0(T)$ should satisfy the relation $dt_0/dT = -R$, which requires the steady-state value of ω to be

$$\omega = \frac{-R}{2d_rC + 2d_i}. \quad (17)$$

This equation can be used to physically explain how the center wavelength of the laser will be shifted in the presence of detuning. Furthermore, from Eq. (14), in order for $\omega(T)$ to have a constant steady-state value, the following inequality needs to be satisfied:

$$|M\omega_M| \geqslant \left|\frac{2d_r(1 + C^2)R}{\tau^2(d_rC + d_i)}\right|. \quad (18)$$

This is the required condition for the synchronous mode-locking solution to exist. It can be used to physically explain why synchronous mode locking cannot be maintained when the detuning R is large enough. Further comparison of the variational solution with the direct simulation results will be described in the next section.

IV. STATE CHANGE ANALYSIS AND DISCUSSION

A. Mode-locking state transition under fixed modulation strength

As shown by the direct simulation results, the mode-locked laser exhibits different operation states under different detuning values. The laser may also become not exactly stable near the transition boundaries. To explain the observed stability of different mode-locking states, we also calculate the averaged steady-state lasing gain g with respect to the constant linear loss l and plot it as a function of the detuning in Fig. 6. Physically, the state that has the lowest steady-state gain should be the most stable one. However, if the required gain differences with respect to other solution states are not large enough, these higher-order solution states may not be damped out quickly enough. Under this situation they can grow significantly due to the transient gain and the stable operation of the original state may be destroyed. Therefore, judging from the gain difference between the operating mode-locked state with respect to the second lowest mode-locked state or the unmode-locked solutions, one should be able to reasonably predict the stability of the mode-locked state [12,27,39,40]. Based on this insight, the results for the case without any nonlinearity ($k_r = 0$, $k_i = 0$) and for the case only without the saturable absorption effect ($k_r = 0$) are also plotted in Fig. 6 for comparison.

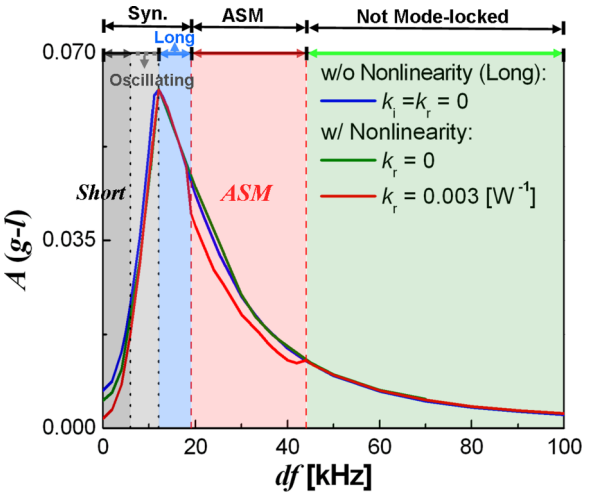

FIG. 6. (Color online) Averaged $g - l$ as a function of df. The red line shows the nonlinear case with $k_i = 0.045\,\mathrm{W}^{-1}$ and $k_r = 0.003\,\mathrm{W}^{-1}$, the green line the nonlinear case with $k_i = 0.045\,\mathrm{W}^{-1}$ and $k_r = 0$, and the blue line the linear case with $k_i = 0$ and $k_r = 0$ (for the long-pulse state).

For the cases without nonlinearity ($k_r = 0$, $k_i = 0$) and without detuning ($R = 0$), from Eq. (13) two steady-state solutions for the pulse chirp can be easily found: $C = -(d_i/d_r) \pm [(d_i/d_r)^2 + 1]^{1/2}$. The two chirp values correspond to the two single-pulse solutions at the valley ($M > 0$) and at the peak ($M < 0$) of the modulation phase, respectively [38]. The steady-state value of the pulse width can also be found from Eq. (16) as

$$\tau = \left[\frac{-8(d_rC + d_i)(1 + C^2)}{M\omega_M^2}\right]^{1/4}. \quad (19)$$

When substituting in the parameters of our example, the value of C is estimated to be -0.19 or 5.19. The low-chirp short pulse is found with $\tau \approx 3.04$ ps at the valley of the modulation phase, while the high-chirp long pulse is with $\tau \approx 6.92$ ps at the peak of the modulation phase. It should be noted that the FWHM pulse width is related to τ by $\tau_{\mathrm{FWHM}} \approx (2\ln 2)^{1/2}\,\tau$. At zero detuning, the short-pulse state exhibits a smaller steady-state lasing gain and thus is the globally stable state. The laser will tend to operate on this short-pulse state. Under small detuning,

the short-pulse state can remain synchronously mode locked by shifting the center frequency linearly with respect to the detuning frequency as predicted by Eq. (17). This gives rise to a quadratic increasing term for the steady-state lasing gain through the bandpass filtering effect. The above picture is still true in the presence of the nonlinear effects, except that the pulse width can be even shorter. This will be identified as the first mode-locking state in the present study. In Fig. 6 the steady-state lasing gain for the longer pulse in the linear case is also plotted for comparison. This is because it can act as an upper bound for the steady-state lasing gain of the first mode-locking state. When the lasing gain of the first mode-locking state is approaching this limit, the laser pulse train will tend to become unstable as seen from direct simulation. After passing the first transition point around 12 kHz in Fig. 6, it is found that only a new chirped long-pulse state can exist. It is identified as the second mode-locking state. The sign of the center frequency shift switches to the opposite side due to the large chirp value. When the detuning is further increased, synchronous mode locking is still maintained by the linear increasing of the pulse width and chirp as shown in Fig. 5. The magnitude of the center frequency shift is actually decreasing. This explains the decreasing of the lasing gain in this regime.

When the detuning is further increased, the nonlinear saturable absorption effect begins to show its importance in forming the stable ASM state. The steady-state lasing gain is significantly lower in the presence of the saturable absorption. This explains why the ASM operation state is found to be very stable both numerically and experimentally. The pure Kerr nonlinearity does not have the same effect, as also shown in Fig. 6. This explains why the ASM operation state was not found experimentally in a pure fiber soliton laser without the equivalent fast saturable absorption. The detuning dependence of the steady-state lasing gain for the ASM state can also be explained physically. In Eq. (14), if the $t_0(T)$ in the expression of m_1 can be ignored when compared to the linear timing drift RT, then the m_1 term is simply a sinusoidal driving term for $\omega(T)$. This gives rise to the sinusoidal oscillation of $\omega(T)$ as given by the approximate solution

$$\omega(T) = \frac{M\sin(\omega_M RT - \phi_d)}{\sqrt{(4d_r)^2/(\omega_M\tau^2)^2 + R^2}},$$
$$\phi_d = \cos^{-1}\left[\frac{4d_r}{\sqrt{(4d_r)^2 + (\tau^2\omega_M R)^2}}\right]. \quad (20)$$

This sinusoidal center frequency oscillation will produce a loss term through the bandpass filtering effect. Its magnitude can be estimated to be equal to the average value of $d_r\omega(T)^2$ in Eq. (12). It is thus expected that for the ASM state, the averaged steady-state lasing gain should exhibit the following trend:

$$A(g-l) \approx \frac{d_r(M f_R f_M)^2}{2[(2d_r f_R)^2/(\pi\tau^2)^2 + df^2]} + c. \quad (21)$$

This equation explains the decreasing of the ASM lasing gain when the detuning is increasing. Eventually, when the detuning is increased up to the point where the ASM steady-state lasing gain is approaching the upper bound set by the linear case as shown in Fig. 6, the ASM state ceases to exist. This explains why there is a detuning upper bound for the stable ASM operation. Instability has also been observed near the transition point between the synchronous long pulse and the ASM states for the same reason.

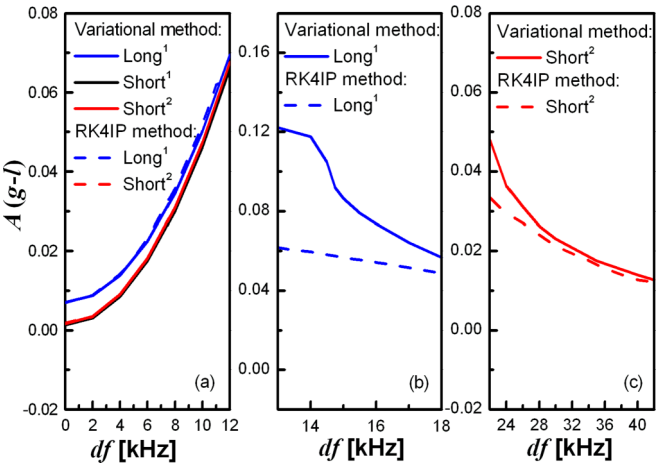

FIG. 7. (Color online) Comparison of the averaged $g-l$ as a function of df between the variational solution (solid lines) and the RK4IP numerical solution (dashed lines) in the (a) first mode-locking region for the long-pulse state (blue) and the short-pulse state (black) without nonlinearity ($k_i = 0$ and $k_r = 0$) and for the short-pulse state (red) with nonlinearity ($k_i = 0.045\,\mathrm{W}^{-1}$ and $k_r = 0.003\,\mathrm{W}^{-1}$), (b) second mode-locking region for the chirped long-pulse state (blue) without nonlinearity ($k_i = 0$ and $k_r = 0$), and (c) third (asynchronous) mode-locking region for the short-pulse state (red) with nonlinearity ($k_i = 0.045\,\mathrm{W}^{-1}$ and $k_r = 0.003\,\mathrm{W}^{-1}$).

In Fig. 7 we perform a quantitative comparison between the variational solution and the direct numerical solution for the same set of equation parameters. In general, the approximate variational solution can correctly predict the dependence of the steady-state lasing gain on the frequency detuning at least qualitatively. This justifies the physical understanding based on the analytic variational pulse parameter equations. For the synchronous short-pulse state, the agreement of the two models is actually very good. This suggests that the assumed single-Gaussian-pulse solution ansatz and the second-order Taylor expansion of the phase modulation function are appropriate in this regime. In contrast, for the synchronous chirped long-pulse state, there are obvious discrepancies in the predicted steady-state gain values and the state transition points. By examining the pulse shape and phase profile example as shown in Fig. 8 from direct numerical solution, one can see that the pulse solution in this regime is obviously with significant higher-order chirps, which are not included in the assumed single-Gaussian-pulse solution ansatz. The origin of these higher-order chirps may be due to the higher-order Taylor expansion terms of the phase modulation function, which are not included in the variational formulation and are expected to become more significant when the pulse width is long. For the asynchronous mode-locking state, the agreement of the two models is better. Since the pulse width of the asynchronous mode-locking state is shorter than that of the synchronous

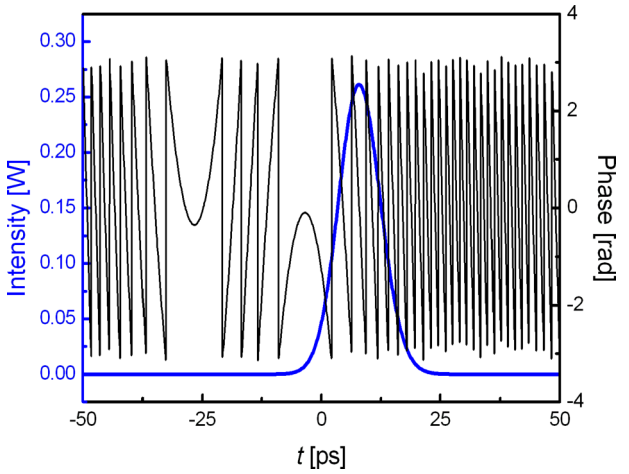

FIG. 8. (Color online) Example of the pulse shape (blue line) and phase profile (black line) from direct numerical solution with the detuning $df = 14$ kHz.

chirped long-pulse state, the impacts of the higher-order Taylor expansion terms for the phase modulation function are expected to be smaller. However, some higher-order chirps can still be observed in the phase profile of the pulse solution and small distortion of the pulse shape occurs when the timing oscillating direction is switched. These explain the medium discrepancies seen in this regime. Because of these discrepancies, direct numerical solution is still needed in order to obtain accurate results.

B. Two-dimensional state transition diagram

The mode-locking state transition of the studied laser is also affected by another important control parameter: the phase modulation strength M. To illustrate this point, we have plotted the two-dimensional transition diagram as illustrated in Fig. 9. It can be clearly seen that the synchronous mode-locking

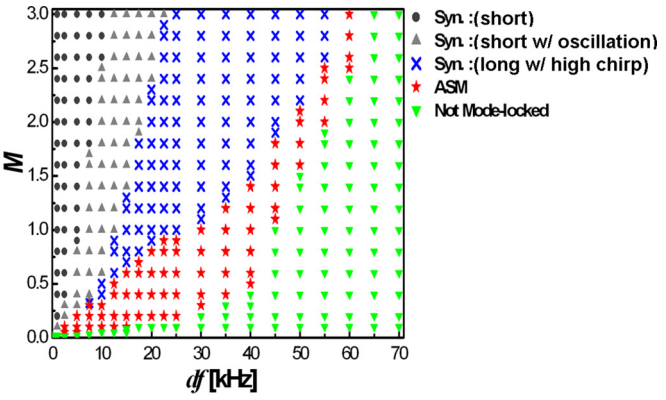

FIG. 9. (Color online) Mode-locking state transition diagram for varying detuning frequency df and modulation strength M: dark gray circles, stable synchronous short-pulse state; gray up-pointing triangles, synchronous short-pulse state with oscillations; blue crosses, synchronous chirped long-pulse state; red stars, asynchronous mode-locking (ASM) state; and bright green down-pointing triangles, non-mode-locked region.

boundaries for both the short- and long-pulse states are moving to larger detuning values almost linearly when the modulation depth is increased. This relation can be physically explained by using the synchronous mode-locking condition in Eq. (18). If the involved pulse parameters remain unchanged, then Eq. (18) predicts the exact linear dependence on the modulation depth. In contrast, the asynchronous to non-mode-locked boundary is only increased with saturation when the modulation depth is increased. The ASM regime is thus reduced when the modulation depth is large. To more physically elucidate this relation, one can estimate the decay rate of the linear long-pulse solution under no detuning and use it to represent the time scale for the laser perturbation to be damped out [27]. Physically this perturbation decay rate should be much faster than the detuning frequency in order for the laser operation state to be stable in the presence of detuning. Thus, an analytic criterion can be derived as shown below, which gives an upper bound for the detuning frequency:

$$f_R \sqrt{\frac{|M|\omega_M^2\left(\sqrt{d_r^2+d_i^2}+|d_i|\right)}{4}} \gg |df|. \qquad (22)$$

One can see that the square-root dependence on the modulation depth is predicted, which explains more physically the observed trend exhibited in the numerical results. When substituting in the parameters, the estimated decay rate is around 56.1 kHz. The calculated upper limit of detuning for the ASM state is $\Delta f_{\text{lim}} \approx 42$ kHz, which agrees reasonably well with the criterion. Such a mode-locking state transition diagram as illustrated in Fig. 9 can provide many useful insights to understand the operation of the studied laser system.

V. CONCLUSION

We have investigated theoretically the laser dynamics of a hybrid mode-locked laser with active phase modulation and passive saturable absorption. The emphasis is on the mode-locking state transition characteristics under the modulation frequency detuning effect. Three distinct mode-locking states (synchronous short-pulse, synchronous long-pulse, and asynchronous short-pulse states) have been identified. The steady-state lasing gain has been utilized to understand and estimate the stability of the mode-locking states. Additionally, their two-dimensional state transition diagram under varying detuned frequency and modulation strength has been calculated and plotted. The obtained results should be very helpful for designing better hybrid mode-locked lasers of this type. Moreover, the theoretical concepts and techniques developed here should also be useful to study other types of mode-locked lasers.

ACKNOWLEDGMENT

This work was supported by the Ministry of Science and Technology in Taiwan under Contract No. MOST 102-2221-E-009-152-MY3.

[1] M. Nakazawa, T. Hirooka, M. Yoshida, and K. Kasai, IEEE J. Sel. Top. Quantum Electron. **18**, 363 (2012).
[2] M. Horowitz, C. R. Menyuk, T. F. Carruthers, and I. N. Duling, J. Lightwave Technol. **18**, 1565 (2000).
[3] G. E. Villanueva, M. Ferri, and P. Pérez-Millán, IEEE J. Quantum Electron. **48**, 1443 (2012).
[4] A. Khilo, S. J. Spector, M. E. Grein, A. H. Nejadmalayeri, G. W. Holtzwarth, M. Y. Sander, M. S. Dahlem, M. Y. Peng, M. W. Geis, N. A. DiLello, J. U. Yoon, A. Motamedi, J. S. Orcutt, J. P. Wang, C. M. Sorace-Agaskar, M. A. Popović, J. Sun, G.-R. Zhou, H. Byun, J. Chen, J. L. Hoyt, H. I. Smith, R. J. Ram, M. Perrott, T. M. Lyszczarz, E. P. Ippen, and F. X. Kärtner, Opt. Express **20**, 4454 (2012).
[5] S. Tozburun, M. Siddiqui, and B. J. Vakoc, Opt. Express **22**, 3414 (2014).
[6] A. G. Podoleanu, J. Lightwave Technol. **28**, 624 (2010).
[7] A. M. Weiner, *Ultrafast Optics* (Wiley, New York, 2009).
[8] H. A. Haus, IEEE J. Sel. Top. Quantum Electron. **6**, 1173 (2000).
[9] L. E. Nelson, D. J. Jones, K. Tamura, H. A. Haus, and E. P. Ippen, Appl. Phys. B **65**, 277 (1997).
[10] N. G. Usechak, G. P. Agrawal, and J. D. Zuegel, IEEE J. Quantum Electron. **41**, 753 (2005).
[11] J. Tu and J. N. Kutz, IEEE J. Quantum Electron. **45**, 282 (2009).
[12] F. X. Kärtner, D. M. Zumbühl, and N. Matuschek, Phys. Rev. Lett. **82**, 4428 (1999).
[13] J. B. Geddes, W. J. Firth, and K. Black, SIAM J. Appl. Dyn. Syst. **2**, 647 (2003).
[14] G. H. C. New, M. Noy, J. A. Crosse, A. Rumley, L. Newson, Z.-Y. Chen, C. Cheung, and A. Todhunter, Opt. Commum. **282**, 4418 (2009).
[15] U. Morgner and F. Mitschke, Phys. Rev. E **58**, 187 (1998).
[16] M. van Hecke, E. de Wit, and W. van Saarloos, Phys. Rev. Lett. **75**, 3830 (1995).
[17] J. Lee and J. H. Lee, J. Opt. Soc. Am. B **30**, 1479 (2013).
[18] A. E. Siegman and D. J. Kuizenga, IEEE J. Quantum Electron. **QE-6**, 803 (1970).
[19] S. E. Harris and O. P. McDuff, IEEE J. Quantum Electron. **QE-1**, 245 (1965).
[20] S. Longhi and P. Laporta, Appl. Phys. Lett. **73**, 720 (1998).
[21] S. Yang, E. A. Ponomarev, and X. Bao, IEEE Photon. Technol. Lett. **16**, 1631 (2004).
[22] K. S. Abedin, N. Onodera, and M. Hyodo, Opt. Commum. **158**, 77 (1998).
[23] S. Longhi and P. Laporta, Phys. Rev. A **60**, 4016 (1999).
[24] S. Longhi and P. Laporta, Phys. Rev. E **61**, R989 (2000).
[25] S. Yang and X. Bao, Phys. Rev. A **74**, 033805 (2006).
[26] C. R. Doerr, H. A. Haus, and E. P. Ippen, Opt. Lett. **19**, 1958 (1994).
[27] H. A. Haus, D. J. Jones, E. P. Ippen, and W. S. Wong, J. Lightwave Technol. **14**, 622 (1996).
[28] W.-W. Hsiang, H.-C. Chang, and Y. Lai, IEEE J. Quantum Electron. **46**, 292 (2010).
[29] S.-S. Jyu and Y. Lai, Opt. Lett. **38**, 347 (2013).
[30] S.-M Wang, S.-S. Jyu, W.-W. Hsiang, and Y. Lai, IEEE Photon. J. **5**, 1500207 (2013).
[31] D. Anderson, Phys. Rev. A **27**, 3135 (1983).
[32] C. Jirauscheck and F. X. Kärtner, J. Opt. Soc. Am. B **23**, 1776 (2006).
[33] C. Antonelli, J. Chen, and F. X. Kärtner, Opt. Express **15**, 5919 (2007).
[34] B. G. Bale and J. N. Kutz, J. Opt. Soc. Am. B **25**, 1193 (2008).
[35] J. Hult, J. Lightwave Technol. **25**, 3770 (2007).
[36] A. M. Heidt, J. Lightwave Technol. **27**, 3984 (2009).
[37] S.-Y. Wu, W.-W. Hsiang, and Y. Lai, J. Opt. Soc. Am. B **31**, 1508 (2014).
[38] N. G. Usechak and G. P. Agrawal, J. Opt. Soc. Am. B **22**, 2570 (2005).
[39] H. A. Haus and A. Mecozzi, Opt. Lett. **17**, 1500 (1992).
[40] F. X. Kärtner, D. Kopf, and U. Keller, J. Opt. Soc. Am. B **12**, 486 (1995).